

Report Title

ABSTRACT

The principal goal of this research is to experimentally measure the three-dimensional transient deformation processes that occur in armor systems undergoing a range of dynamic loading conditions. The development of a 3-D image correlation system using digital cameras capable of acquiring images every 5 nano-seconds were used. Due to the nature of the cameras, extensive algorithms for the removal of image distortions were required. The image correlation technology was transferred to army personnel through a 1 year sabbatical at ARL's Aberdeen research facility by the principal investigator.

List of papers submitted or published that acknowledge ARO support during this reporting period. List the papers, including journal references, in the following categories:

(a) Papers published in peer-reviewed journals (N/A for none)

Surendranath H., Bruck H.A., Gowrisankaran, S., "Enhancing the Optimization of Material Distributions in Composite Structures Using Gradient Architectures", International Journal of Solids and Structures 40, 2999-3020 (2003)

Sutton M.A., Li N., Garcia D., Cornille N., Orteu J.J., McNeill S.R., Schreier, H., Li, X., "Metrology in SEM: Theoretical Developments and Experimental Validations" accepted for publications in Measurement Science and Technology

Surendranath H., Bruck H.A., Gowrisankaran, S., "Enhancing the Optimization of Material Distributions in Composite Structures Using Gradient Architectures", accepted for publication in the International Journal of Solids and Structures.

Sutton M.A., Li N., Garcia D., Cornille N., Orteu J.J., McNeill S.R., Schreier, H., Li, X., "Metrology in SEM: Theoretical Developments and Experimental Validations" accepted for publication in Measurement Science and Technology

M.L. Pines and H.A. Bruck "Pressureless Sintering of Particle-reinforced Metal-Ceramic Composites for Functionally Graded Materials: Part II. Sintering Model", Acta Materialia (IF=3.430), 54, 1457-1465 (2006).

M.L. Pines and H.A. Bruck, "Pressureless Sintering of Particle-reinforced Metal-Ceramic Composites for Functionally Graded Materials: Part I. Porosity Reduction Models", Acta Materialia (IF=3.430), 54, 1457-1465 (2006).

Y.M. Shabana, M.L. Pines, and H.A. Bruck, "Modeling the Evolution of Stress Due to Differential Shrinkage in Powder-Processed Functionally Graded Metal-Ceramic Composites During Pressureless Sintering", accepted for publication in International Journal of Solids and Structures

Y.M. Shabana, H.A. Bruck, V. Giurgiutiu, B. Xu, and M.A. Sutton, "Characterization and Modeling of Stiffness Evolution in Sintered Metals and Ceramics", in preparation (2005).

Y.M. Shabana, M.L. Pines, H.A. Bruck, B. Xu, and J.P. Laskis, "Modeling the Evolution of Elastic Mechanical Properties During Pressureless Sintering of Powder-Processed Metals and Ceramics for Functionally Graded Materials", submitted to Journal of Materials Science

Number of Papers published in peer-reviewed journals: 9.00

(b) Papers published in non-peer-reviewed journals or in conference proceedings (N/A for none)

"Development and Use of a High Speed Optical System for Deformation Measurements", SEM X International Congress, Costa Mesa, CA, June 2004 (with S.R. McNeill, M.A. Sutton and W. Zhao)

"Application of Ceramics as Performance Enhancers for Armor Systems", SEM X International Congress, Costa Mesa, CA, June 2004 (S.R. McNeill, V. Tiwari and M.A. Sutton)

"Measurement Errors Consideration for using an Ultra-High Speed for Digital Image Correlation" 12th International Conference on Experimental Mechanics, August 2004, Politecnico di Bari, Italy (S.R. McNeill, R. Sands, V. Tiwari and M.A. Sutton)

M.L. Pines, H.A. Bruck, and Y.M. Shabana, "Powder Processing of Functionally Graded Metal-Ceramic Plates using Pressureless Sintering", Proceedings of the 2004 SEM X International Congress and Exposition on Experimental and Applied Mechanics, Costa Mesa, CA, 1-5 (2004)

Number of Papers published in non peer-reviewed journals: 4.00

(c) Papers presented at meetings, but not published in conference proceedings (N/A for none)

H.A. Bruck, “Biologically Inspired Functionally Graded Materials”, Technical Meeting on the Mechanics of Biological and Biologically Inspired Materials, Springfield, MA, 10/03.

“Characterization of Impact Damage Evolution in Functionally Graded Composites using Novel Nanosecond 3D Deformation Measurement System” 16th US Army Symposium on Solid Mechanics, Charleston, SC, May 2003 (with S.R.McNeill, M.A.Sutton, Y.J.Chao and H.A.Bruck)

Number of Papers not Published: 2.00

(d) Manuscripts

Number of Manuscripts: 0.00

Number of Inventions:

Graduate Students

NAME	PERCENT SUPPORTED	
Scott Williams	0.50	No
Vikarant Tawair	0.50	No
Micahe L Pines	0.50	No
Jon Krufft	0.50	No
FTE Equivalent:	2.00	
Total Number:	4	

Names of Post Doctorates

NAME	PERCENT SUPPORTED
FTE Equivalent:	
Total Number:	

Names of Faculty Supported

NAME	PERCENT SUPPORTED	National Academy Member
Stephen R McNeill	0.13	No
Michael A Sutton	0.13	No
Hugh A Bruck	0.13	No
FTE Equivalent:	0.39	
Total Number:	3	

Names of Under Graduate students supported

NAME	PERCENT SUPPORTED
FTE Equivalent:	
Total Number:	

Names of Personnel receiving masters degrees

<u>NAME</u>	
Michael L Pines	No
Scott Williams (expected Dec 2006)	No
Jon Kruft (expected Dec 2006)	No
Total Number:	3

Names of personnel receiving PHDs

<u>NAME</u>
Total Number:

Names of other research staff

<u>NAME</u>	<u>PERCENT SUPPORTED</u>
FTE Equivalent:	
Total Number:	

Sub Contractors (DD882)

Inventions (DD882)

Table of Contents

Statement of problem studied.....	2
Accomplishments.....	2
Appendix	
Technology Transfer.....	3
Sabbatical at ARL by Dr. McNeill.....	4
Paper on distortion correction for SEM.....	11

Statement of problem studied

The principal goal of this research was to develop a system to experimentally measure the three-dimensional transient deformation processes that occur in multi-layer, functionally graded ceramic (CMC's) armor systems undergoing a range of dynamic loading conditions. The development of the metrology system presented unique challenges to the researchers which required significant development.

Accomplishments

The ultra-high speed IMACON200 cameras have unique optics that presents unexpected challenges for their use with digital image correlation. Although not perceivable when images are viewed on a monitor, imaging warping and shearing have been measured when using digital image correlation with a single IMACON200 camera to measure uniform, in-plane translations. Through a detailed study of the imaging process and the associated errors, we have developed a basic understanding for the source of the errors. Working with a local company specializing in optical methods, experimental techniques and associated software have been developed to characterize the cameras and improve the image correlation measurements.

The techniques developed for the IMACON 200 cameras and their unique optics have been shown to work in all imaging system that has distortion. The scanning electron microscope is a device which has unique distortions which must be overcome if it is to be used for metrology purposes. The techniques developed have the ability to allow the SEM to be used for metrology in regards of deformation on small scales. The personal at ARL's facility in Aberdeen Maryland have expressed interest in the use of this method. The paper which discusses this is attached to the final report since it has been accepted but not yet published.

Manufacturing techniques have been refined to properly produce the functional graded ceramic-metallic materials. Initial samples were produced and tests of the samples for the required consistency and integrity is ongoing, with preliminary results indicating that samples can be produced reliably. For example, two material interface samples were produced and delivered to USC for initial experimental setup and verification. Papers have been published on the functionally graded material and processing requirements and are listed in the paper published section.

Initial imaging using the ultra-high speed cameras of the 2D impact of the two material interface samples were obtained using the cameras in a 2-D configuration. The experimental parameters developed for this application include proper triggering, camera control during impact process and specimen lighting. Due to large distortions in the experimental system the results were inclusive and work will be ongoing to evaluate these specimens.

Technology Transfer

A tour of our laboratory-scale impact facility was given to Bruce Fink, Chief, Materials Division, Army Research Laboratory. During the tour, a high speed impact event was captured by a single IMACON200 camera, and the images converted into deformation fields with our new software. He expressed his strong support for the development process and stated that he “sees tremendous potential in the application of this technology to a wide variety of efforts involving rate-dependent properties of materials and high-rate testing of military structures.”

Conversations and a meeting at a professional society conference have been had with Dr, Tusit Weerasooriya, of the Impact Physics Branch of Army Research Laboratory. He has stated “Once the system is developed, we intend to use it, with USC collaboration, in our high rate lab”. He has given a few examples where they intend to use the system which included

- Measuring the back surface deformation of personnel armor during impact to validate computational models.
- To develop valid test techniques to measure high rate behavior of ceramics and soft polymers. These materials are extremely difficult to test under high rates using traditional experimental techniques.
- Measure fracture behavior of penetrator rods.

The experimental work involves the use of 3-D image correlation developed by a small, start-up, high tech measurements company, Correlated Solutions, Inc. (CSI). As the first graduate from the USC Incubator program, the company is now located a few miles from the campus of the University of South Carolina and has been supportive of the on-going research activities in the experimental mechanics group at USC. Currently, we are working closely with CSI personnel in the development of unique software needed to control the ultra-high speed cameras and analyze the resulting images. Correlated Solutions plans to market systems using this unique software.

We worked with Dr. Dave McGowen of NASA-Langley’s Structures and Materials Division to make dynamic structural measurements using the ultra-high speed 3D measurement system that is being used in this work.

Dr. McNeill's sabbatical at ARL's facility at Aberdeen Maryland

Many of the experimental techniques developed for this work was of great interest to researchers at ARL's facility at Aberdeen Maryland. Dr. McNeill spent all of 2005 at ARL transferring the technology and helping with problems of interest to the ARL researchers. Below is a list of some of the projects and their results that was worked on by Dr. McNeill during the sabbatical.

Project # 1: Determination of stress strain properties for green bullet system

In an effort to reduce the potential long-term environmental effects that may accrue due to the use of lead in ballistic applications, the US Army has begun development of new ballistic materials that have similar material properties to the lead currently being used. Compression testing is being performed on various materials that have the same size and shape of the lead core they are replacing. The specimens being tested are 4.6 mm in diameter and 6.4 mm in length.

Significant Contributions

All experimental data was obtained as the specimen incurred elastic deformation. Full-field displacement and strain measurements were obtained using 3D Digital Image Correlation, pioneered at the University of South Carolina. Prior to the use of Digital Image Correlation, the specimens were instrumented with strain gauges and tested in a standard compression load frame. The time required to instrument each specimen with strain gauges was over one hour due to the small size of the specimens being studied. As a result, only a few specimens could be instrumented and tested per day. With digital image correlation, many specimens could be speckled in a matter of a few minutes and then tested. Using 3D digital image correlation it was possible to speckle and test specimens at a rate of three per hour, improving the through-put of the experimental program while also developing full-field data to determine the overall response of the green bullet material under compressive loading.

Project # 2: Small Disk Impact

A commonly used impact experiment employs a small flat round specimen. The specimen is placed perpendicular to the muzzle of a gas cannon and then impacted by a spherical projectile. Analysis of the specimen consists of measuring the height of the deformation after impact. Since no strain information has been available in the past, only qualitative data has been obtained previously.

Significant Contribution

All experiments were performed using 3D digital image correlation, a technique pioneered at the University of South Carolina. Both surfaces of the specimen were speckled and images obtained prior to being placed in the gas gun fixture. After

impact, the specimen was removed and images obtained. Then, the images were analyzed using digital image correlation software, so that the following data was obtained

(a) the complete 3D shape of the final surface

(b) the complete surface deformation fields on both surfaces is obtained after impact

Figure 1 shows the measured shape of the surface opposite to the impact. Figure 2 shows the measured shape of the impacted surface; note that there was data obtained at the impact site, allowing investigators to acquire new measurement data heretofore unobtainable. Figure 3 shows the radial strain field after impact on the surface opposite to the impact.

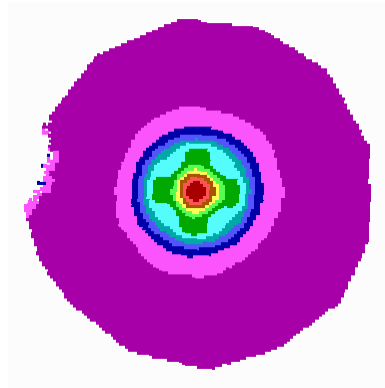


Figure 1: Radial strain calculated using strains from 3D image correlation

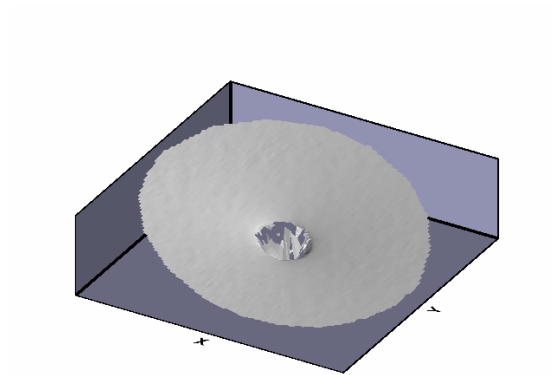


Figure 2: Profile of impact side after impact

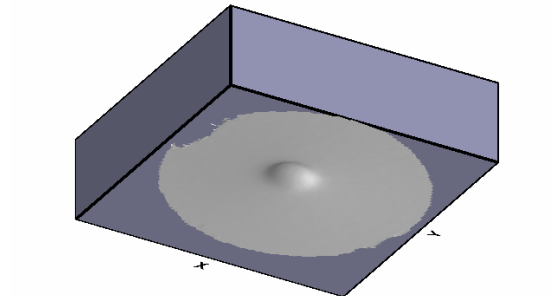


Figure 3: Profile of opposite side from impact after impact

Project # 3: Dynamic Deformation Measurements in Kevlar Fabric During Impact

There has been a paucity of data for validation of existing computational models to predict the deformation process in Kevlar fabric undergoing projectile impact loading.

Significant Contribution

To obtain the first set of dynamic data, two high speed cameras were placed in a stereo-vision arrangement and images were acquired during the impact event. 3D digital image correlation, pioneered at the University of South Carolina, was used to analyze a series of images acquired during impact.

Two sets of experiments were performed. One set of experiments was performed at ARL using their gas cannon. A second set of experiments were performed on an ATC test range with projectile velocities exceeding 1,000 m/s.

Typical results are shown in Figure 4. The surface shape during impact is clearly shown in Fig. 4. In addition, the lagrangian strain field is also shown in color contours directly on the deformed surface. As can be seen in Fig. 4, data is obtained throughout the visible region on the specimen surface.

Due the quality of the data obtained, discussions are being held for performing additional 3D deformation measurements during ballistic impact of helmets currently being worn by US soldiers.

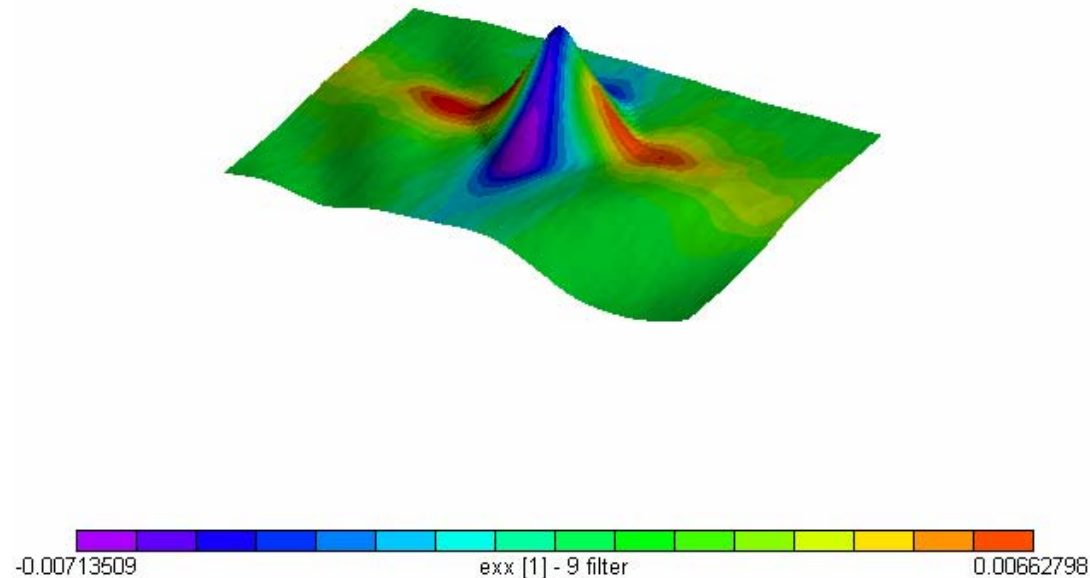


Figure 4: One component of the normal surface strain measured in a Kevlar sheet during impact

Project # 4: High speed deformation measurements of EM gun barrel during charging and discharging

The deformation measurement of the barrel of the electro-magnetic gun during a full charging and discharging cycle would be helpful to understand how the gun is performing during operation. However, methods were not available that were capable of acquiring these measurements.

Significance of the Contribution

To obtain the first set of dynamic data, two high speed cameras were placed in a stereo-vision arrangement and images acquired of the EM gun barrel during a complete charging and discharging cycle. After the images were acquired, 3D digital image correlation, pioneered at the University of South Carolina, was used to analyze a series of the images. Deformations were acquired as the EM gun was subjected to operating currents ranging from 500 kA to 800 kA.

Figure 5 shows the measured radial strain on the barrel of the EM gun at the end of the cycle. As shown in Fig 5, the radial strain field is not symmetric and there is an unexpected large strain area near the edge of the rail; the location of the embedded rail is between the two white lines in Fig 5. The measured strain fields have resulted in investigations into the fabrication techniques used to build the gun

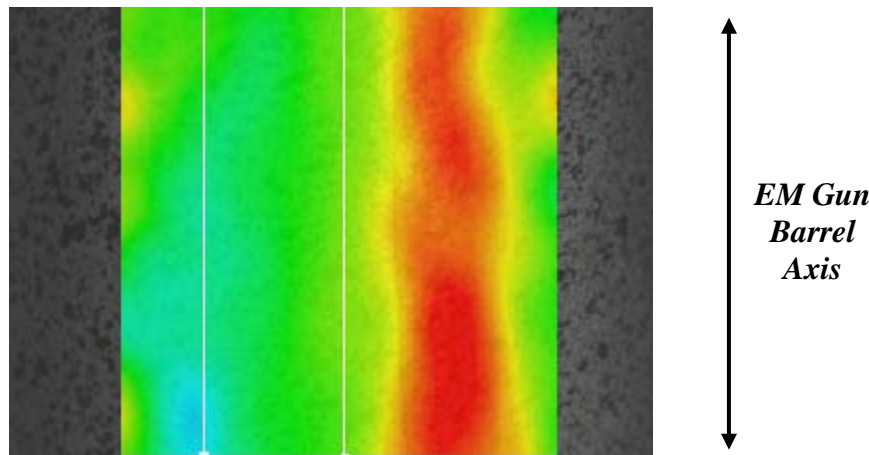


Figure 5: Full field radial strain during discharging

The strain for one point on the barrel as a function of time for various charge voltages is shown in the Figure 6. This data suggests that the EM gun barrel underwent in-elastic deformation during the 800 kA cycle.

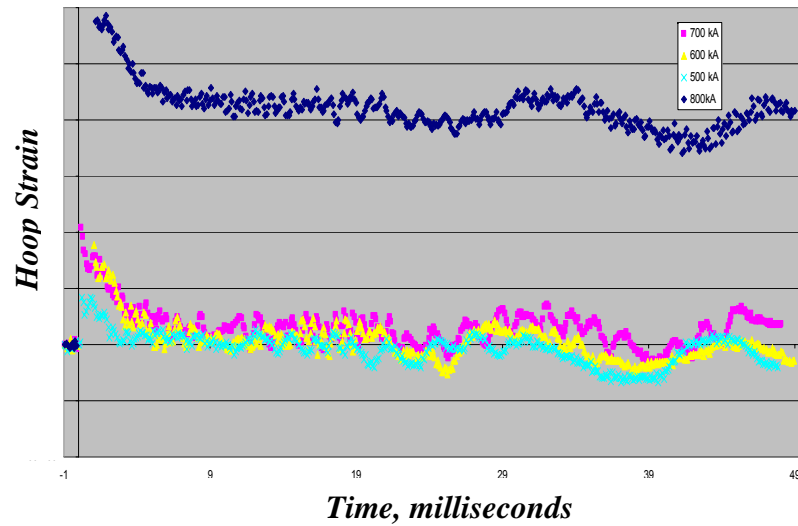


Figure 6: Hoop strain vs time for one point of EM gun

Metrology in SEM: Theoretical Developments and Experimental Validation

Michael A. Sutton¹, Ning Li¹, Dorian Garcia², Nicolas Cornille³,

Jean Jose Orteu³, Stephen R. McNeill¹, Hubert W. Schreier², Xiaodong Li¹

Abstract

A novel approach for correcting both spatial and drift distortions that are present in scanning electron microscope (SEM) images is described. Spatial distortion removal is performed using a novel methodology employing a series of in-plane rigid body motions and a generated warping function. Drift distortion removal is performed using multiple, time-spaced images to extract the time-varying relative displacement field throughout the experiment.

Results from numerical simulations clearly demonstrate that the correction procedures successfully remove both spatial and drift distortions. Specifically, in the absence of intensity noise the distortion removal methods consistently give excellent results with errors on the order of ± 0.01 pixels.

Results from the rigid body motion and tensile loading experiments at 200X indicate that, after correction for distortions, (a) the displacements have nearly random variability with standard deviation of 0.02 pixels; (b) the measured strain fields are unbiased and in excellent agreement with previous full-field experimental data obtained with optical illumination; (c) the strain field variability is on the order of 60 microstrain in all components with a spatial resolution on the order of 25 pixels.

Taken together, the analytical, computational and experimental studies clearly show that the correction

¹ Department of Mechanical Engineering, University of South Carolina, Columbia, SC 29208, Sutton@sc.edu.

² Correlated Solutions, Inc, 952 Sunset Boulevard, West Columbia, SC 29252.

³ Ecole des Mines d'Albi, Albi, France.

procedures successfully remove both spatial and drift distortions while retaining excellent spatial resolution, confirming that the SEM-based method can be used for both micro-material and nano-material characterization in either the elastic or elastic-plastic deformation regimes.

1. Introduction

Computer vision and digital image correlation (DIC) have been applied to the study of in-plane material behavior at the macro-scale^[1-4]. For nominally planar objects undergoing in-plane motions, the 2D-DIC technique became one of the preferred optical methods for measurements in experimental mechanics. For general surface shapes with arbitrary motions, 3D-DIC (stereo-vision) employing at least two views to recording object positions has been shown to have general capability to measure 3D shape and full-field 3D motions^[5-13]. Nowadays, 2D and 3D methods using computer vision are widely used in many applications, and commercial software is available^[14].

A first step to access a reduced-length scale of measurement is to apply the DIC method with images obtained using high-magnification optical systems for 2D or 3D measurements^[15-17]. Few authors have investigated the problem of the accurate calibration of micro-scale imaging systems, including the determination and correction of the underlying distortions in the measurement process. One reason may be the obvious complexity of high-magnification imaging systems that weakens the underlying assumptions commonly used in parametric distortion models that correct simple lens systems such as digital cameras^[18, 19].

Recently, Schreier et al. proposed a new methodology to calibrate accurately any imaging sensor by correcting *a priori* for the distortion using a non-parametric model^[13]. The *a priori* correction of distortion transforms the imaging sensor into a virtual, distortion-free sensor plane using unknown arbitrary rigid body motions of a gridless planar target. As opposed to classical calibration techniques relying on a dedicated target marked with fiducial points, this approach can be applied using any randomly textured planar object (i.e., a “speckle pattern”). This type of distortion depends only on the pixel location in the image and is designated as spatially-varying distortion or spatial distortion in this work.

Due to the nature of light, optical imaging systems are limited to a maximum resolution that corresponds to a magnification of $\approx 1,000X$. For higher spatial resolution (and also smaller displacements), imaging systems based on

electron microscopy (such as SEM and TEM) are employed. Since the physics of electron microscopy ^[20, 21] is quite different from optical microscopy, a new model and calibration process is necessary compared to the classical approach. For example, SEM systems have both *spatial distortion* and also a time-varying distortion or *drift distortion*. Drift distortion occurs in an SEM imaging system since the electron beam scanning process oftentimes results in a non-uniform “apparent” displacement field across the specimen; relative motions occur between pixel locations that have been shown to change with time. The cumulative effect of both *spatial* and *drift distortions* can introduce large image displacements and substantial image deformations.

To correct for the combined effect of spatial and drift distortion, different projection models have been established but no work has provided both a satisfactory model and a correction method for such image distortions. In fact, most papers and even commercial SEM measurement systems simply ignore these effects and consider a pure projection model ^[22-28]. A few authors taking into account distortion consider only a parametric model ^[29-31] and neglect the effect of drift ^[32-37].

In this paper, the procedure we have developed for quantifying time-varying distortion (Section 2.1) and spatially-varying distortion (Section 2.2) is presented, along with an overall procedure for implementing the distortion determination procedure (Section 2.3). Section 3 describes computer simulations performed to demonstrate the potential accuracy of the method when employed to identify and remove typical *spatial and drift distortion fields*. Section 4 describes the translation and uniaxial strain experiments performed in an SEM to demonstrate the accuracy of the methods developed.

2. Image Distortions in an SEM

It is assumed that there are two independent distortion functions. First, $\mathbf{D}_{dr}(t)$ is defined as the drift distortion function, where t is the scan time and $t \in [0, \infty)$. Second, $\mathbf{D}_{sp}(x, y)$ is defined as the spatial distortion function, where (x, y) is a pixel

location on the image plane.

A position is distorted due to both drift and spatial distortion in an SEM image. Since distorted positions are the measurable quantities in experiments, the inverse functions for both drift and spatial distortion are the quantities that are determined during the calibration process⁴.

2.1. Time-Varying Distortion

Time-varying distortion or drift distortion occurs throughout the scan process, introducing artificial relative displacements as the image is formed, resulting in errors when computing strains using the drift-distorted images; we have observed relative displacements within a single image of up to 6 pixels at 10,000X though relative drift of 0.80 pixels across an image is more common. Because of its non-stationary nature (magnitude and direction are a function of time), this effect cannot be removed when performing spatial distortion correction.

To quantify the drift distortion at each pixel throughout an experiment, a novel drift correction procedure has been developed and is described in the following sections.

2.1.1.SEM Scanning Basics

A SEM image is generated through a raster-scanning process. Each pixel requires a dwell time, t_D , to define the “intensity” of image at that location, so that the time required to scan an entire row, t_R , and an entire frame, t_F , of image are given by

⁴ Though the focus of this study is 2D-DIC with a single view, the procedure should be applied to each camera (view) in a multi-camera system to remove distortions from individual views. Thus, the procedure is equally important when 3D reconstruction are performed using SEM images.

$$t_R = Wt_D + t_J \quad (1)$$

$$t_F = Ht_R = HWt_D + Ht_J \quad (2)$$

where W is the number of columns in the image, H is the number of rows in the image and t_J is the time delay to reposition and stabilize the electron beam prior to initiating the next row scan. Since the (x,y) position in the image is in direct correspondence with the scan time, one can write

$$t(x,y) = xt_D + yt_R \quad (3)$$

where $0 \leq x \leq W-1$ and $0 \leq y \leq H-1$.

Eq. (3) implies that two pixel locations, and hence two distinct scan times, will generally experience much different drift functions. Such differences have been observed for consecutive rows in an image, with a clearly-defined shift in drift measured when moving from the last pixel in one row to the first pixel in the next row.

In order to correct SEM images for drift, three approaches have been investigated: (a) global model of the drift function developed with the data from all images to correct for the drift at (x,y) positions in every image; (b) local time-based models, $\mathbf{D}_{dr}(t)$, that are different for each image and (c) local spatial-based models, $\mathbf{D}_{dr}(x,y)$, that are also different for each image. It is noted that (b) and (c) imply that the drift distortion will only be known locally and must be re-estimated when a new image is acquired. This “incremental” procedure to determine drift distortion correction requires that corrections be made throughout the experimental process, and is in contrast with spatial distortion, which is determined during the calibration phase and does not require re-estimation during the post-calibration phase of an experiment.

Preliminary experiments and comparison of experimental observations to model predictions clearly indicate that the global model cannot adequately represent experimental observations whereas both of the local model predictions are in

good agreement with experimental measurements. In the following sections, only the two local models will be discussed in more detail.

2.1.2. Time-based Local Model

The drift distortion function is expressed as follows

$$\mathbf{D}_{dr}(t) = [\delta_x(t), \delta_y(t)], \quad \text{units in pixels} \quad (4)$$

where t is given in Eq. (3) for a point of interest in the image, (x,y) .

Consider a object point \mathbf{P} located at position (x,y) in the image plane at time t . At time $t+\Delta$, the image of the object point is located at a new position, \mathbf{P}' , due to drift.

The difference in positions for the same object point is the disparity, \mathbf{disp}_{dr} , and can be written in the form

$$\mathbf{disp}_{dr} = \mathbf{D}_{dr}(t+\Delta) - \mathbf{D}_{dr}(t) \quad (5)$$

with

$$t = xt_D + yt_R$$

$$\Delta = t_F + \Delta t_n + t_{disp}$$

$$t_{disp} = [\delta_x(t+\Delta) - \delta_x(t)]t_D + [\delta_y(t+\Delta) - \delta_y(t)]t_R$$

where Δt_n is the delay time between one image scan and the next image scan. Fig. 1 shows a schematic of the process mathematically described by Eqs. (4-5), with the experimentally-observed shift between images clearly visible since the drift for position $(W-1,H-1)$ is not similar to the drift for position $(0,0)$ in the next image.

From the drift evolution shown in Fig. 1, different functional forms can be assumed to represent the local drift. Fig. 1 shows an estimated linear fit to the drift data for three images. The linear fit will smooth regions with high gradients in drift, especially those positions where step changes may occur during the image acquisition process.

To determine the fitting parameters for the assumed form of the drift distortion function, two consecutive images are taken at each step in the experiment. Assuming that only drift occurs between the two images in each consecutive image pair, the drift velocity, $\mathbf{v}_{dr}(t)$, at each position is determined by the disparity in each pair divided by the time increments.

$$\mathbf{v}_{dr}(t+\Delta/2) = \{ [\delta_x(t+\Delta) - \delta_x(t)]/\Delta, [\delta_y(t+\Delta) - \delta_y(t)]/\Delta \} \quad (6)$$

where Δ is defined for pixel (x,y) in Eq. (5) and the disparity values are obtained in the sensor plane.

Advantages of the time-based approach are its direct relationship to the actual scanning process and the relative simplicity of the data-fitting process for time-streamed disparity data. Disadvantages are as follows. First, there are gaps in the time-history due both to the re-positioning of the electron beam after each row scan and to the time delay between acquisitions of images. Second, the drift data in actual experiments exhibits step changes in magnitude during the time-gaps, resulting in difficulties in extracting accurate results near these positions. Third, finite sized subsets in image matching process will introduce averaging effects across the scanned rows, introducing errors in the time-based approach.

2.1.3. Hybrid Spatial-Temporal (HST) Local Model

As shown in Eqs. (3-5), the drift function can be written in terms of spatial variables, the integer pixel position (X_I, Y_J) . The elapsed time during the whole imaging process for calibration can be written as

$$t = X_I t_D + Y_J t_R + (n-1)(t_F + \Delta t_n), \quad n=1,2,\dots,N \quad (7)$$

where N is the total number of images for the drift function estimation.

In this form, one can write $\mathbf{D}_{dr}(X_I, Y_J)$ as the total drift function and $\mathbf{disp}_{dr}(X_I, Y_J)$ as the disparity. The overall imaging process for the HST model is:

- A specimen is patterned so that the SEM images are appropriate for image correlation.

- A sequence of image pairs is acquired. They are numbered as (1,2), (3,4),..., (n-1,n),..., (N-1,N), where drift occurs between image n-1 and n in an image pair.
- Between the acquisition of each image pair, rigid body motions are applied (these will be used to quantify the spatial distortion field).
- For each image pair, 2D-DIC is performed⁵ to determine the drift disparity, **disp**_{dr}(X_i,Y_j), for each fixed position (X_i,Y_j) in the sensor plane.
- A B-spline function is used to obtain a least-square best fit surface to the components of **disp**_{dr}(X_i,Y_j) for each image pair.
- With known values for t_D, t_R and t_F, along with recorded values for Δt_n between each image, Eq. (7) can be used to determine the elapsed time associated with position (X_i,Y_j) in each image. Using Eq. (6), the velocity of drift for each position, **v**_{dr}(X_i,Y_j;t+Δ/2), can be estimated using a central finite difference form.
- At each position (X_i,Y_j), **v**_{dr}(X_i,Y_j;t) is fitted with a B-spline function in time.
- Using the initial condition **D**_{dr}(0,0)=(0,0) at t=0, the B-spline approximation for **v**_{dr}(X_i,Y_j;t) can be integrated over time to determine the drift for each position (X_i,Y_j) in the nth image⁶, **D**_{dr,n}(X_i,Y_j), n=1,3,...,N-1.
- **D**_{dr,n}(X_i,Y_j) is used to correct images n=1,3,...,N-1, for the drift distortion.

Mathematically, the determination of the time dependent drift function for each fixed position (X_i, Y_j) is obtained via

⁵ When using spatially-based drift correction, the subset size should be as small as possible without introducing non-uniqueness in the matching process, thereby minimizing local averaging.

⁶ For the initial image pair, variations in disparity across the image requires a piecewise integration over the disparity field between (0,0) and (X_i,Y_j) so that the drift at any position (X_i,Y_j) can be determined. A less accurate approach would be to integrate the estimated **disp**_{dr}(X_i,Y_j;t) from t=0 to the time corresponding to (X_i,Y_j).

minimization of the following functional

$$\Phi = \sum_{n=1}^N \left| \mathbf{v}_{\text{dr}}(X_I, Y_J; t_n) - \mathbf{v}_{\text{dr}}^{\text{fit}}(X_I, Y_J; \mathbf{a}_j, t_n) \right|^2 \quad (8)$$

where \mathbf{a}_j are the parameters to be fitted and t_n is the elapsed time associated with each drift disparity at the integer pixel position (X_I, Y_J) . To obtain the total drift function at each position

$$\mathbf{D}_{\text{dr}}(X_I, Y_J; t) = \int_0^t \left[\mathbf{v}_{\text{dr}}^{\text{fit}}(X_I, Y_J, \mathbf{a}_j, t) \right] dt, \quad \text{where } \mathbf{D}_{\text{dr}}(0, 0; 0) = \mathbf{0} \quad (9)$$

Once the drift distortion is known as a function of time for each pixel position in each image, this field is fitted by a piecewise B-spline to provide a functional form for each image, $\mathbf{D}_{\text{dr},n}(x,y)$, where (x,y) is any real-valued position in the image.

The HST model described above offers one major advantage: the spatial description of drift within each image minimizes the effects of time gaps on local estimates of the drift function.

2.2. Spatially-varying Distortions

In simple lens systems, such as used in a digital camera, spatially-varying distortion or spatial distortion (a.k.a., image distortion) is a well-known problem. The commonly used method for modeling such imaging systems assumes that the distortions are not a function of time. Classical models used to estimate the spatial distortions are parametric in nature ^[38]; typical model forms include radial distortion, de-centering distortion, prismatic distortion and tangential distortion.

Since the SEM imaging process is based upon the interaction between atoms of the observed specimen and an electron beam, as well as scanning and focusing processes that employ electro-magnetic principles to perform the

required functions, it is clear that the pre-specified classical distortions are likely to be ineffective in quantifying arbitrary aberrations or unknown (but deterministic) distortions in a complex imaging system.

To address this issue, non-parametric forms for distortion models are preferred. Two of the earliest such models are proposed by Peuchot^[39] and Brand et al.^[40], where cross-targets with known spatial separation are used for the distortion estimation. Since such targets are likely to be difficult to realize at the micro- or nano-scale for the SEM, the work of Schreier et al. using a non-parametric distortion correction approach and a speckle-patterned calibration target^[13] is the most readily adaptable for distortion correction in an SEM, and is employed in previous work^[41] as well as in this study.

As outlined by Schreier et al.^[13], the process uses images acquired during translation along two orthogonal directions and B-splines or other general forms to determine full-field, spatial distortions. Here, it is assumed that the procedures outlined in Section 2.1.3 have been employed to remove drift distortions from all of the translated images.

2.3. Overall Process for Distortions Removal

The procedure used in this study to extract drift and spatial distortions is shown as a flow chart in Fig. 2. The pairs of images are separately correlated throughout the calibration phase and measurement phase to obtain the “drift” at selected pixel positions. The resulting drift disparity fields are used to obtain the drift velocity at selected pixel positions throughout the field of view. Using the velocity field as estimates for the local time derivatives, B-spline fits are obtained for the drift distortion.

After removing the estimated drift distortion from each pixel position, the spatial distortion field and rigid body motions during the calibration phase are determined through an optimization procedure. Relaxation principles are

employed during the iteration process to verify that the estimated drift and spatial distortion fields are converged⁷.

3. Numerical Simulations

Simulations are performed for both calibration phase and measurement phase⁸ in consistent with actual experimental conditions. The image correlation process is not simulated. Both drift and spatial distortion functions are assumed to have pre-defined forms. Using these functional forms, the distorted positions of a finite number of locations, $(x,y)_k$, are determined for each image n . The process is repeated at N times, so that the distorted positions $(x,y)_{kn}$, $k=1,2,\dots,K$, $n=1,2,\dots,N$, are determined⁹. This data forms the basis for the simulation process, with the long term goal of demonstrating the accuracy and robustness of the approach for SEM image analysis.

3.1. Simulation for the Calibration

With $\Delta t=120s$, $t_D=10^{-4}s$, $t_R=1.071\times 10^{-2}s$ and an imaging array size of 1024×884 , the positions of image points at 30 specific times (corresponding to 15 image pairs in an experiment) are generated over a total time of 128 minutes. Between each image pair, the effect of a cross-shaped translation is included in the position of each point. To distort the position of each image point, the drift distortion function $\mathbf{D}_{dr}(t)$ is assumed to have a quadratic form. The spatial distortion function is assumed to have the form of a combination of cosine wave and quadratic surface. Fig. 3 shows the drift and

⁷ SEM images and the corresponding disparity maps have considerable electronic and measurement noise. Thus, the HST local drift correction model should employ a reduced order for the B-spline fit to the disparity data so that smoothing of the data is performed during the fitting process so that oscillations in the estimated velocity field are minimized.

⁸ The procedure whereby the drift distortion is computed separately for the calibration and measurement phases is used in practice to minimize the effects of specimen shifts during the initial loading process. However, in principle the process can be continuous.

spatial distortion functions. Thus, with the inclusion of random error, the distorted positions of an image point (x,y) in image n are written

$$\mathbf{P}'(x,y;t) = \mathbf{P}(x,y;t) + \mathbf{D}_{dr}(x(t),y(t)) + \mathbf{D}_{sp}(x,y) + \mathbf{G}(x(t),y(t)) \quad (10)$$

where $\mathbf{G}(x,y)$ is a Gaussian error function with mean value $\mathbf{0}$ and a pre-defined standard deviation, varying with time and by Eq. (3) spatial position (x,y).

Instead of performing correlation to extract the disparity maps, a total of $150 \times 120 = 18,000$ distorted positions with a spacing of 5 pixels and a “beginning” image position located at (101,101) are calculated using Eq. (10) with known vectors on the right hand side.

To obtain the drift component numerically, all 15 drift disparity maps are computed at each pixel location and Eqs. (6-10) are applied to extract $\mathbf{D}_{dr}(x,y)$. Fig. 4 shows a direct comparison between the computed and the input drift at position (511,441). Fig. 5 shows the spatial distribution for the difference between the computed and the input vertical drift for the image acquired at t=36 minute.

After correction to remove the effects of drift, the disparity maps are obtained by subtracting the positions of points in the reference image, image 1, from the positions of matching points in all other odd-numbered images. The resulting disparity maps have the form

$$\mathbf{disp}_{sp}(x,y) = \mathbf{D}_{sp}(x+u,y+v) - \mathbf{D}_{sp}(x,y) + \mathbf{G}(x,y) \quad (11)$$

where (u,v) is the orthogonal rigid body motion of other images relative to image 1.

By incorporating the computed disparity maps into Eq. (10), the procedure described in [13] is employed to perform

⁹ In practice, 7 to 11 pairs of images are acquired during the calibration phase; the only requirement is that several translations in two orthogonal directions be performed. The number of pairs of images during the measurement phase will vary with the number of strain increments; for better estimation of B-Spline function it should be more than 6 pairs of images acquired.

least-square bundle-adjustment optimization and determine all translations and all parameters in the spatial distortion function. Fig. 6 shows the difference between the computed and the input spatial distortion.

As a final check on the accuracy of the drift and spatial distortion correction method, the residual strain fields (with and without Gaussian noise in the displacement values) are computed for all of the images within the calibration phase. Without Gaussian noise in the displacement components, the computed strains are less than 1 microstrain throughout the entire sequence. With Gaussian noise having a standard deviation ≈ 0.025 pixels in each displacement component, all strains have an *average* strain between ± 60 microstrain and a standard deviation ≈ 50 microstrain.

3.2. Discussion

The simulations assumed a total drift of 10-20 pixels over 2 hours. Thus, between images in the sequence, the drift is relatively small and the local drift velocities can have considerable oscillation due to electronic noise. Even so, the simulations confirmed that the method proposed will give good overall accuracy, even in the presence of substantial Gaussian noise in the measurements, when combining both drift and spatial distortion correction.

Since the drift is relatively small between images, it may appear that one can simply ignore this phenomenon. However, our simulations indicate that ignoring or incorrectly estimating drift distortion will introduce substantial errors in the spatial distortion correction. These errors will introduce large residual strains ($\approx 1,000$ microstrain) that cannot be removed from the data.

4. Experiment Validation for Calibration and Strain Measurement

4.1. Experimental Setup

Consistent with results obtained in the previous sections, all SEM imaging in this paper is performed using an FEI

Quanta-200 SEM in high vacuum mode. For the electron beam, (a) the accelerating voltage is 30KV, (b) beam spot size is 3, (c) $t_D=10^{-4}$ s, (d) $t_R=1.071\times 10^{-2}$ s. The CCD sensor array has a size of 1024×884. These data corresponds to $t_F=94.67$ s. All images are obtained using the BSE detector with a working distance 14.3mm. For validation purposes, a magnification of 200X is used, which corresponds to $\approx 1.25\mu\text{m}$ per pixel. The intensity value is stored in 8-bits format in the file.

To apply a micro-scale pattern to the specimen, the procedure described in previous publications^[42-46] is used. For comparison to the vision-based measurements, a single strain gage is aligned with the loading direction. All experiments are performed with the specimen installed in a tensile loading frame and mounted inside the SEM chamber.

4.2 Experiments

The first experiment corresponds to the calibration phase and requires a series of translations in two orthogonal directions performed manually via external motion controls. The second experiment adds a series of strained images that correspond to the measurement phase; uniaxial loading is performed in load control using a Labview control and data acquisition program.

After completing each experiment and acquiring all images, the disparity maps are obtained by 2D-DIC using a specially modified version of commercial software VIC2D^[14]. All correlations are performed at 150×120 image locations using a 43×43 subset size and spacing between subset centers of 5 pixels, the first subset center is at (101,101). Thus, all disparity maps contain 18,000 points.

The procedures outlined in Fig. 2 are employed to determine the drift and spatial distortion functions. To obtain strain fields from the corrected displacement data, local quadratic fits to the displacement components are performed.¹⁰

¹⁰ In this case, the spatial resolution is governed by the subset size. An estimate for the spatial resolution is ≈ 25 pixels.

4.3. Calibration Phase--Drift and Spatial Distortions Removal

A cross-shaped motion path is performed with 16 motions. Before beginning the motion sequence, two consecutive images are acquired as “references”, resulting in a total of 17 pairs of images for calibration.

Fig. 7 shows the measured drift velocity in y-direction (dv/dt) at location (236,211), along with the best-fit quadratic function. Though oscillations are clearly present (noise is on order of ± 0.02 pixels), they are small and only visible due to the relatively small drift velocity of 0.01 pixels/minute measured in the SEM at this magnification.

The measured spatial distortion functions are presented in Fig. 8. Here, it is clear that the spatial distortions are much larger than the expected drift distortions, with spatial distortion corrections up to 1 pixel in x-direction and 2 pixels in y-direction.

The strain fields are also computed in each of the 16 calibration images. Results indicate that

- the *uncorrected* ϵ_{xx} , ϵ_{yy} and ϵ_{xy} have average values approaching 200 microstrain and a standard deviation of 100 microstrain.
- the *drift-corrected* ϵ_{xx} , ϵ_{yy} and ϵ_{xy} have average values between 100 and 200 microstrain and a standard deviation of 80 microstrain.
- the *spatial distortion-corrected* ϵ_{xx} , ϵ_{yy} and ϵ_{xy} have average values near 50 microstrain and a standard deviation of 60 microstrain.
- the *fully-corrected* ϵ_{xx} , ϵ_{yy} and ϵ_{xy} have average values near zero and a standard deviation of 60 microstrain.

4.4 Measurement Phase--Application of Uniaxial Tension

After completing the calibration phase, the specimen is subjected to increasing uniaxial loading and images are acquired at 6 different load levels. To minimize the potential for unwanted image motion, after increasing loading on the specimen each time, a hold time of 30s is maintained prior to acquiring additional images.

To obtain the additional drift components that accumulate during the strain portion of the experiment, the procedures outlined Section 2.1.3 are employed to extract the drift corrections during the loading sequence. Both the spatial distortion and also the new local drift functions are used to correct all spatial positions during the loading process. The disparity maps are acquired across corrected odd-numbered images to determine the residual deformation field.

Table 1 presents a summary of the average data across the field, along with estimates for the variability of each strain component. The data in Table 1 indicates that the shear strain is nearly zero throughout the experiment and the standard deviation within the field is less than 114 microstrain for all components.

Fig. 9 presents the average strain data for ϵ_{xx} (transverse to loading direction) and ϵ_{yy} (along loading direction) at all loading levels, along with a direct comparison to the independently measured ϵ_{yy} data via strain gage. As shown in Fig 9, the average data from strain gage and our fully-corrected data are in excellent agreement, confirming that the Young's modulus obtained from the strain gage measurements and the fully-corrected data are nearly the same, 70GPa. This value is consistent with a wide range of literature values for aluminum alloys.

Also shown in Fig. 9 are the strain values that would be predicted using (a) no corrections and (b) drift correction only. It is clear that fully-corrected images are necessary for accurate strain estimation so that reasonable estimates can be made for elastic material response.

Finally, since Poisson's ratio, ν , is defined by $\nu = -\epsilon_{xx} / \epsilon_{yy}$, the average measured value using fully corrected image correlation images is 0.33. This is in good agreement with handbook data, which has a range $0.29 < \nu < 0.34$.

4.5. Discussion

Algorithms implementing both spatial and drift distortion correction method have been shown to be effective for removing distortions from SEM images. Thus, the data clearly indicates that basic elastic material properties can be reasonably quantified using digital image correlation with corrected SEM images. Furthermore, even at low magnification, both corrections are essential for accurate measurement of elastic response.

The methods outlined in this work have been extended by the authors to make quantitative, high accuracy 3D displacement and shape measurements with an SEM^[47], the complete development will be the subject of forthcoming articles. For such measurements, the equations of 3D computer vision replace the relatively simple 2D equations given in Section 2, and the calibration phase described previously^[13] is employed where the specimen is rotated about its eucentric axis to obtain multiple views, and image correlation is employed to locate a dense set of matching positions in a component. By several measured 3D profile of some objects using stereo images obtained in our SEM, though no quantitative comparison is provided, the results are encouraging and provide confidence that, when completed, the method will be both accurate and robust in such applications.

5. Concluding Remarks

The novel method outlined in this work relies on a combination of a priori drift and spatial distortion correction so that accurate elastic and elastic-plastic deformation measurements can be obtained using SEM images; both corrections are essential to obtain accurate deformation measurements throughout the field of view.

In sharp contrast with the approach of early SEM measurements, where the investigators simply accepted the accuracy obtainable and successfully performed their studies for important problems amenable to such limitations, this

work presents a general approach that successfully extends the range of measurements obtainable in an SEM to the small deformation (elastic) regime so that full elastic-plastic deformation studies can be performed in an SEM.

Simulation results have shown that typical drift processes in an SEM can be adequately reconstructed using local drift velocity measurements. However, if higher gradients in drift are present during the early stages of image acquisition, the simulations also show that image acquisition time should be reduced and additional images need to be acquired during this period for accurate drift reconstruction, a situation that may not be feasible with a given microscope. In practice, image acquisition should be conducted 15-30 minutes after the first image scan is initiated so that the gradients in drift are reduced to a more manageable level.

6. Acknowledgements

The support of (a) the National Science Foundation, Dr. Oscar Dillon and Dr. Kenneth Chong through grant CMS-0201345, (b) Intel and Michael Mello through grant DOCC-22860, (c) the Army Research Laboratory and Dr. Adam Rawlett through Cooperative Agreement W911NF0420026 and (d) the Ecole des Mines d'Albi (France) who provided a grant for Nicolas Cornille is gratefully acknowledged. The technical assistance provided by Dana Dunkelberger and Dr. Donggao Zhao in the USC Electron Microscopy Center, as well as their financial support of this research, is deeply appreciated.

7. References

- [1] W.H. Peters and W.F. Ranson; Digital Imaging Techniques in Experimental Stress Analysis; Optical Engineering, 21(3):427-432, 1982.
- [2] S.R. Mc Neill, M.A. Sutton, W.J. Wolters, W.H. Peters and W.F. Ranson; Determination of Displacements Using an

- Improved Digital Correlation Method; Image and Vision Computing, 1(3):1333-1339, 1983.
- [3] T.C. Chu, W.F. Ranson, M.A. Sutton and W.H. Peters; Application of Digital Image Correlation Techniques to Experimental Mechanics; Experimental Mechanics, 25(3):232-244, 1985.
- [4] M.A. Sutton, M. Cheng, W.H. Peters, Y.J. Chao and S.R. McNeill; Application of an Optimized Digital Correlation Method to Planar Deformation Analysis; Image and Vision Computing, 4(3):143-153, 1986.
- [5] Z.L. Khan-Jetter and T.C. Chu; Three-Dimensional Displacement Measurements Using Digital Image Correlation and Photogrammic Analysis; Experimental Mechanics, 30(1):10-16, 1990.
- [6] P.F. Luo, Y.J. Chao and M.A. Sutton; Application of Stereo Vision to 3D Deformation Analysis in Fracture Mechanics; Optical Engineering, 33:981-990, 1994.
- [7] J.D. Helm, S.R. McNeill and M.A. Sutton; Improved 3D Image Correlation for Surface Displacement Measurement; Optical Engineering, 35(7):1911-1920, 1996.
- [8] J.J. Orteu, V. Garric and M. Devy; Camera Calibration for 3-D Reconstruction: Application to the Measure of 3-D Deformations on Sheet Metal Parts; European Symposium on Lasers, Optics and Vision in Manufacturing; Munich, Germany, June, 1997.
- [9] P. Synnergren and M. Sjodahl; A Stereoscopic Digital Speckle Photography System for 3D Displacement Field Measurements; Optics and Lasers in Engineering, 31:425-443, 1999.
- [10] K. Galanulis and A. Hofmann; Determination of Forming Limit Diagrams Using an Optical Measurement System; 7th International Conference on Sheet Metal, 245-252; Erlangen, Germany, September, 1999.
- [11] M.A. Sutton, S.R. McNeill, J.D. Helm and H.W. Schreier; Computer Vision Applied to Shape and Deformation Measurement; International Conference on Trends in Optical Nondestructive Testing and Inspection, 571-589; Lugano, Switzerland, May, 2000.

- [12] D. Garcia; Mesure de formes et de champs de déplacements tridimensionnels par stéréo-corrélation d'images; PhD thesis, Institut National Polytechnique de Toulouse, France; December, 2001.
- [13] H.W. Schreier, D. Garcia and M.A. Sutton; Advances in Light Microscope Stereo Vision; Experimental Mechanics, 44(3):278-288, 2004.
- [14] Correlated Solutions Inc.; VIC2D and VIC3D; 952 Sunset Blvd., W. Columbia, SC 29252; www.correlatedsolutions.com.
- [15] M.A. Sutton, T.L. Chae, J.L. Turner and H.A. Bruck; Development of Computer Vision Methodology for the Analysis of Surface Deformations in Magnified Images; MiCon 90: Advances in Video Technology for Micro-structural Control, editor George F. Van Der Voort, American Society for Testing and Materials, ASTM STP 1094:109-132, 1990.
- [16] E. Mazza, G. Danuser and J. Dual; Light Optical Measurements in Microbars with Nanometer Resolution; Microsystem Technologies 2:83-91, 1996.
- [17] H.L. Mitchell, H.T. Kniest and O. Won-Jin; Digital Photogrammetry and Microscope Photographs; Photogrammetric Record, 16(94):695-704, 1999.
- [18] H A Beyer; Accurate Calibration of CCD-cameras; International Conference on Computer Vision and Pattern Recognition (CVPR'92), 96-101; Champaign-Urbana, IL, USA, June, 1992.
- [19] J. Weng, P. Cohen and M. Herniou; Camera Calibration with Distortion Models and Accuracy Evaluation; IEEE Transactions on Pattern Analysis and Machine Intelligence 14:965-980, 1992.
- [20] D.C. Joy; The Theory and Practice of High-Resolution Scanning Electron Microscopy; Ultramicroscopy, 37:216-233, 1991.
- [21] D.C. Joy, Ko Y-U and Hwu JJ; Metrics of Resolution and Performance for CD-SEMs; Proc. SPIE Vol. 3998, p. 108-114, Metrology, Inspection, and Process Control for Microlithography XIV, Neal T. Sullivan; Ed., 2000.

- [22] MeX software; Alicona Imaging; www.alicon.com.
- [23] SAMx; 3D TOPx package; www.samx.com.
- [24] M. Hemmleb, J. Albertz, M. Schubert, A. Gleichmann and J.M. K; Digital Microphotogrammetry with the Scanning Electron Microscope; International Society for Photogrammetry and Remote Sensing, 1996.
- [25] A.J. Lacey, N.A. Thacker and R.B. Yates; Surface Approximation from Industrial SEM Images; British Machine Vision Conference (BMVC'96), 725-734; 1996.
- [26] M. Agrawal, D. Harwood, R. Duraiswami, L. Davis and P. Luther; Three-Dimensional Ultrastructure from Transmission Electron Microscope Tilt Series; 2nd Indian Conference on Vision, Graphics and Image Processing (ICVGIP 2000); Bangalore, India, 2000.
- [27] F. Vignon, G. Le Besnerais, D. Boivin, J.L. Pouchou and L. Quan; 3D Reconstruction from Scanning Electron Microscopy Using Stereovision and Self-calibration; Physics in Signal and Image Processing; Marseille, France, June, 2001.
- [28] O. Sinram, M. Ritter, S. Kleindiek, A. Schertel, H. Hohenberg and J. Albertz; Calibration of an SEM, Using a Nano Positioning Tilting Table and a Microscopic Calibration Pyramid; ISPRS Commission V Symposium, 210-215; Corfu, Greece, 2002.
- [29] P. Doumalin; Microextensométrie locale par corrélation d'images numériques; PhD thesis, Ecole Polytechnique, 2000.
- [30] M. Hemmleb and J. Albertz; Microphotography -- The Photogrammetric Determination of Friction Surfaces; IAPRS XXXIII; Amsterdam, The Netherlands, 2000.
- [31] H.S. Lee, G.H. Shin and H.D. Park; Digital Surface Modeling for Assessment of Weathering Rate of Weathered Rock in Stone Monuments; The International Archives of the Photogrammetry, Remote Sensing and Spatial Information

Sciences; Ancona, Italy, July 2003.

- [32] J.W. Dally and D.T. Read; Scanning Moiré at High Magnification Using Optical Methods; *Experimental Mechanics*, 33(1):110-116, 1993.
- [33] J.W. Dally and D.T. Read; Scanning Moiré at High Magnification Using Electron Beam; *Experimental Mechanics*, 33(4):270-277, 1993.
- [34] J.R. Berger, E.S. Drexler and D.T. Read; Error Analysis and Thermal Expansion Measurement with Electron-Beam Moiré, *Experimental Mechanics*, 38(3):167-171, 1998.
- [35] Z.Y. Zhang; A New Multistage Approach to Motion and Structure Estimation by Gradually Enforcing Geometric Constraints; *Asian Conference on Computer Vision (ACCV'98)*, 567-574; Hong Kong, China, January, 1998.
- [36] O. Ravn, N.A. Andersen and A.T. Sorensen; Auto-calibration in Automation Systems using Vision; *3rd International Symposium on Experimental Robotics (ISER'93)*, 206-218; Kyoto, Japan, October, 1993.
- [37] J.M. Lavest, M. Viala and M. Dhome; Do We Really Need an Accurate Calibration Pattern to Achieve a Reliable Camera Calibration? *5th European Conference on Computer Vision (ECCV'98)*, 158-174; Freiburg, Germany, June, 1998.
- [38] D.C. Brown; Lens Distortion for Close-Range Photogrammetry; *Photometric Engineering*, 37(8):855-866, 1971.
- [39] B. Peuchot; Camera Virtual Equivalent Model 0.01 Pixel Detector; *Computerized Medical Imaging and Graphics*, 17:289-294, 1993.
- [40] R. Brand, P. Mohr and P. Bobet; Distorsions optiques: corrections dans un modèle projectif; *9th Congress AFCET, Reconnaissances des Formes et Intelligence Articielle (RFIA'94)*, 87-98; Paris, France, January, 1994.
- [41] N Cornille; Accurate 3D Shape and Displacement Measurement Using a Scanning Electron Microscope, PhD thesis, Ecole des Mines d'Albi (France)/University of South Carolina, 2005.

- [42] S.A. Collette, M.A. Sutton, P. Miney, A.P. Reynolds, X.D. Li, P.E. Colavita, W.A. Scrivens, Y. Luo, T. Sudarshan, P. Muzykov and M.L. Myrick; Development of Patterns for Nanoscale Strain Measurements: I. Fabrication of Imprinted Au Webs for Polymeric Materials; *Nanotechnology*, 15:1812-1817, 2004.
- [43] W.A. Scrivens, Y. Luo, M.A. Sutton, S.A. Collette, M.L. Myrick, P. Miney, P.E. Colavita, A.P. Reynolds and X.D. Li; Development of Patterns for Digital Image Correlation Measurements at Reduced Length Scales; in press for special issue on Nano-scale Measurements in the *International Journal for Experimental Mechanics*.
- [44] M.A. Sutton, W. Zhao, S.R. McNeill, J.D. Helm, W.T. Riddell and R.S. Piascik; Local Crack Closure Measurements: Development and Application of a Measurement System Using Computer Vision and a Far-Field Microscope; K. Smith and J. McDowell, Ed., *ASTM STP 1343 on Crack Closure Measurements*, 145-156, 1999.
- [45] W.T. Riddell, R.S. Piascik, M.A. Sutton, W. Zhao, S.R. McNeill and J.D. Helm; Determining Fatigue Crack Opening Loads from Near-Crack-Tip Measurements; K. Smith and J. McDowell, Ed., *ASTM STP 1343 on Crack Closure Measurements*, 157-174, 1999.
- [46] N. Cornille, H.W. Schreier, D. Garcia, M.A. Sutton, S.R. McNeill and J.J. Orteu; Gridless Calibration of Distorted Visual Sensors; *Colloque Photoméchanique*; Albi, France, May, 2004.

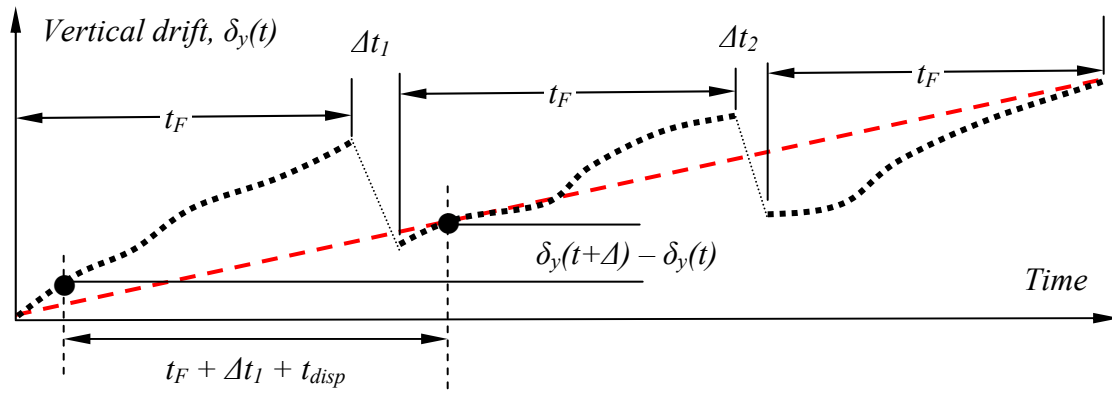


Fig. 1 Schematic representation for noiseless vertical drift as a function of time for three images, along with definition of disparity. Dashed line represents a best linear fit.

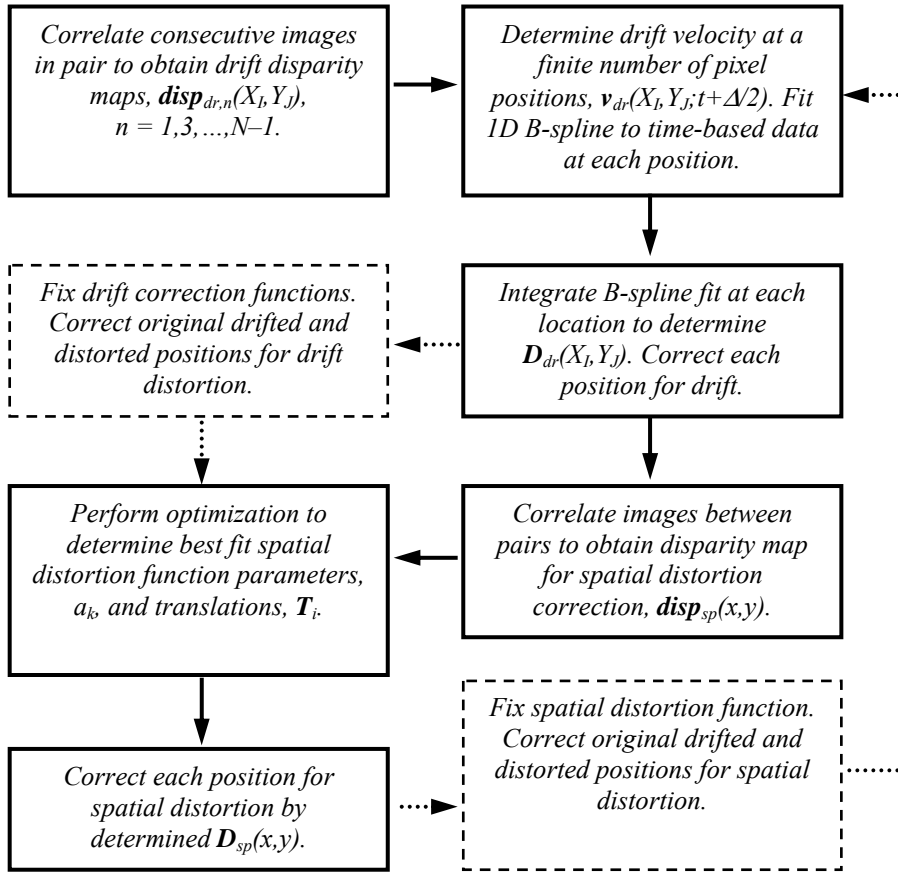


Fig. 2 Overall procedure employed for correcting distortion in an SEM. Relaxation methods are implemented during process to improve convergence.

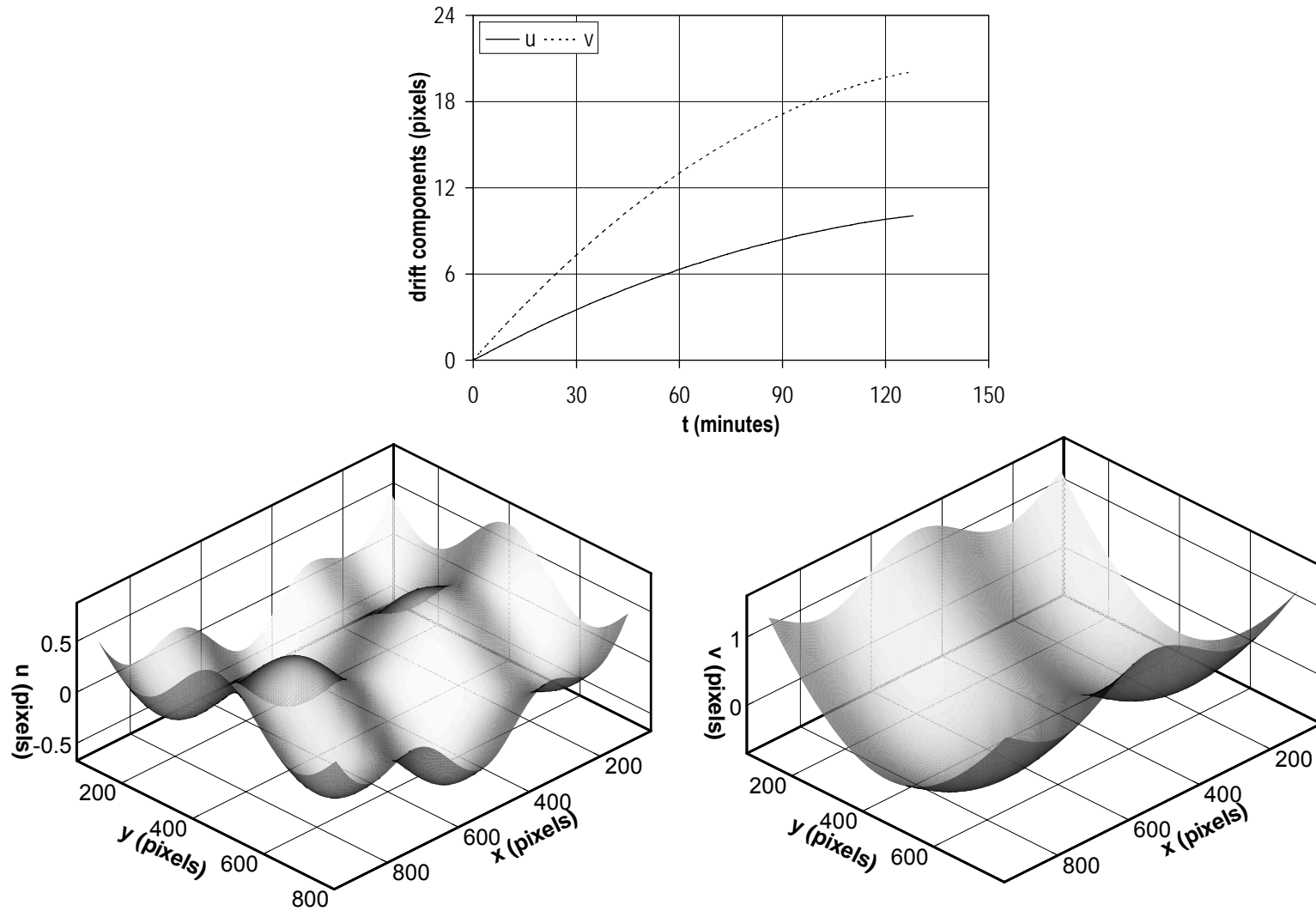


Fig. 3 Drift distortion and spatial distortion components for computer simulations. With spatial distortion ranging from -0.5 to +1 pixels and drift ranging up to 20 pixels over 2 hours.

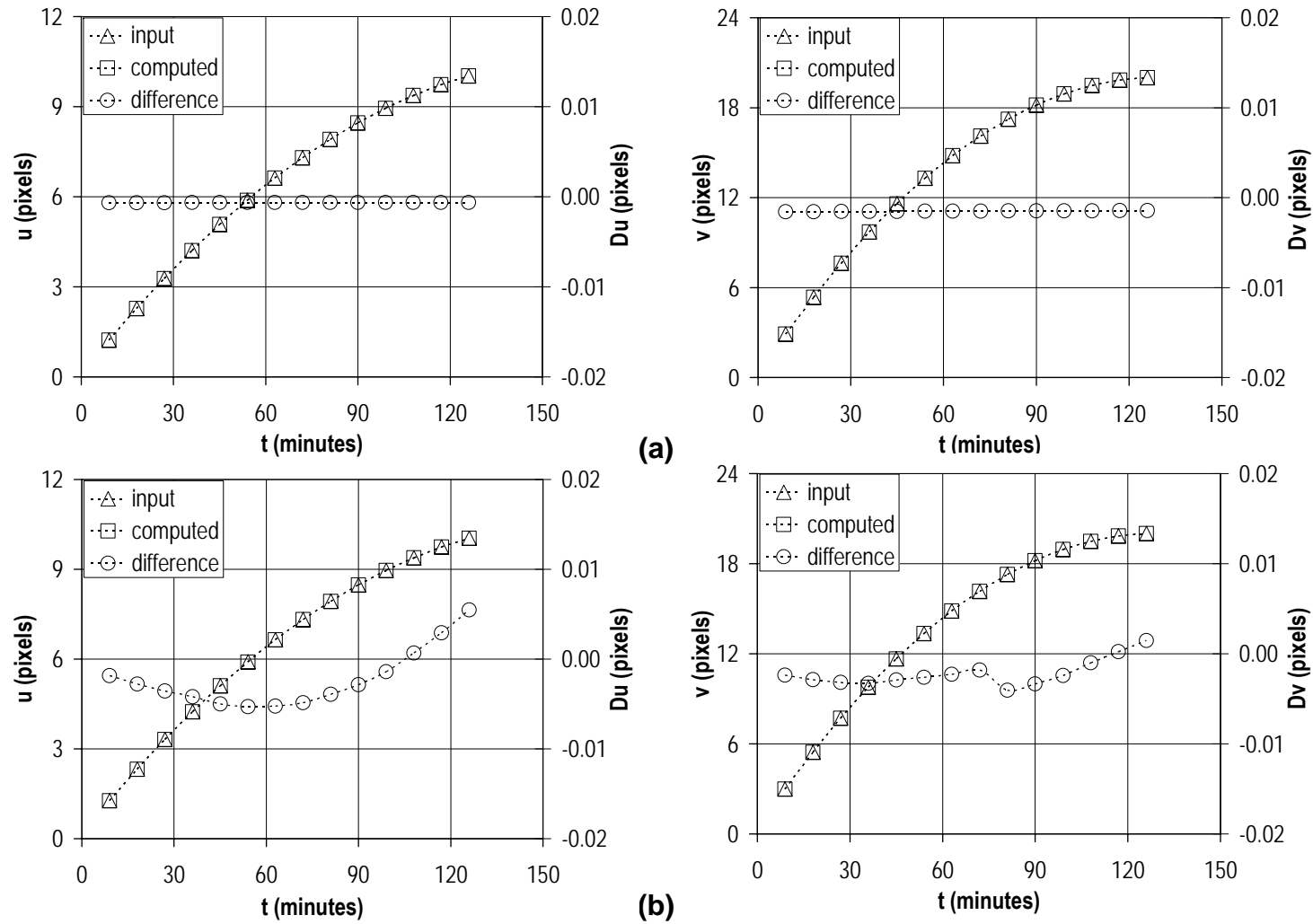


Fig. 4 Comparison of the computed and the input drift at pixel (511,441) throughout calibration process (a) without Gaussian noise and (b) with Gaussian noise range of ± 0.1 pixels added to the measurements.

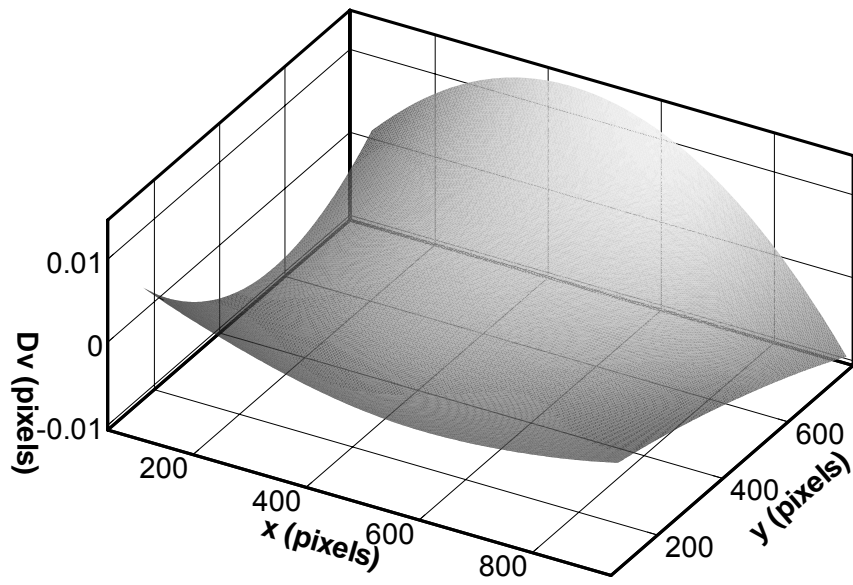


Fig. 5: Spatial distribution of difference between computed and input vertical drift for the image acquired at $t=36$ minute.

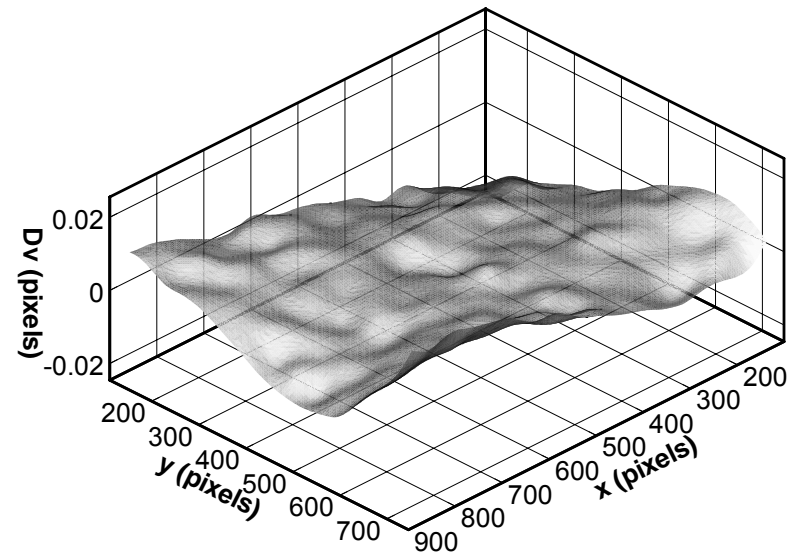
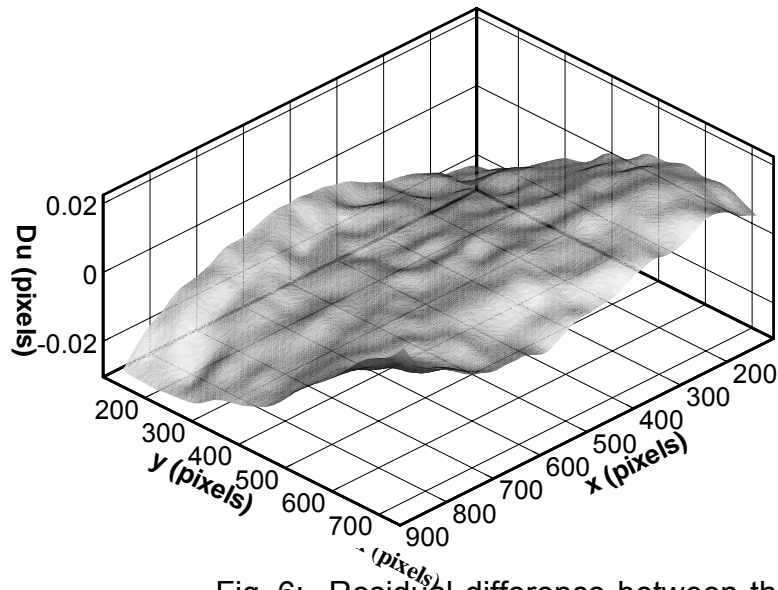


Fig. 6: Residual difference between the computed and the input distortion. Gaussian noise of ± 0.1 pixels applied to input data. Residuals are less than ± 0.02 pixels throughout the field.

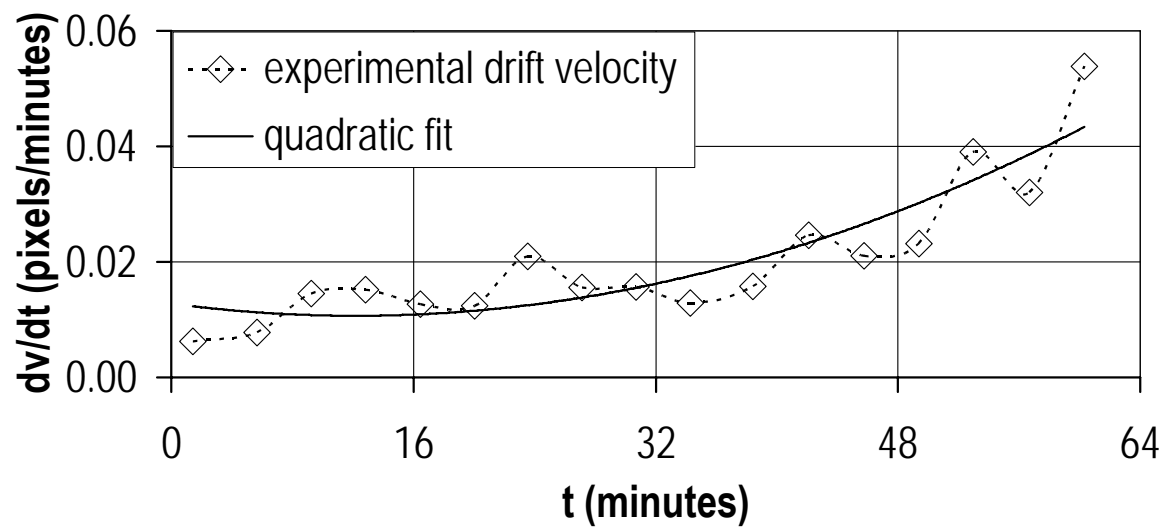


Fig. 7: Measured drift velocity as a function of time at a fixed pixel location (236,211) during the calibration phase along with quadratic fit. Data shown is typical of all locations throughout the field.

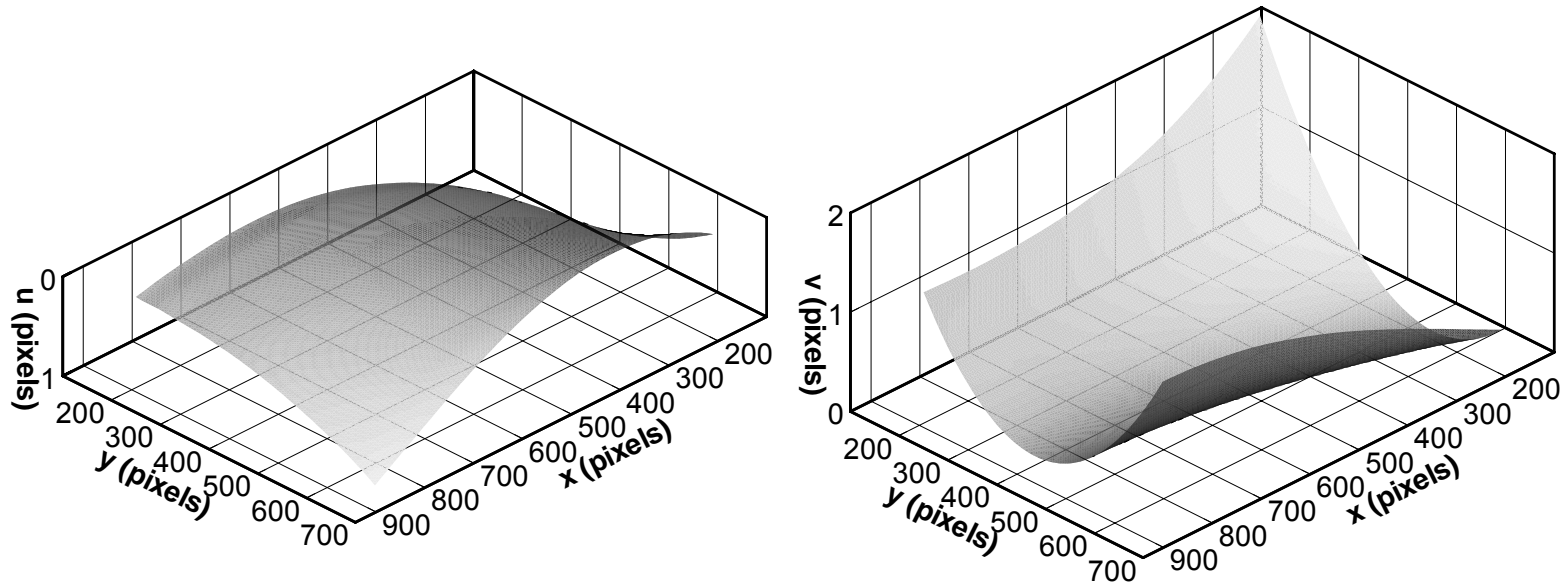


Fig. 8: Measured spatial distortion fields. Note the larger gradients in the vertical distortion field.

<i>Relative Time to the First Image (min)</i>	<i>ϵ_{xx} Average ($\times 10^{-6}$)</i>	<i>ϵ_{xy} Average ($\times 10^{-6}$)</i>	<i>ϵ_{yy} Average ($\times 10^{-6}$)</i>	<i>ϵ_{xx} Standard Deviation ($\times 10^{-6}$)</i>	<i>ϵ_{xy} Standard Deviation ($\times 10^{-6}$)</i>	<i>ϵ_{yy} Standard Deviation ($\times 10^{-6}$)</i>
5.0	-83	-10	350	54	38	62
9.9	-249	-26	677	41	53	51
14.9	-387	-48	956	53	71	63
19.9	-446	-32	1290	114	94	71
24.7	-457	-27	1573	105	108	78
29.8	-631	1	1850	87	110	81

Table 1: Strain data obtained using fully corrected SEM images acquired at seven times during the uniaxial tension loading process.

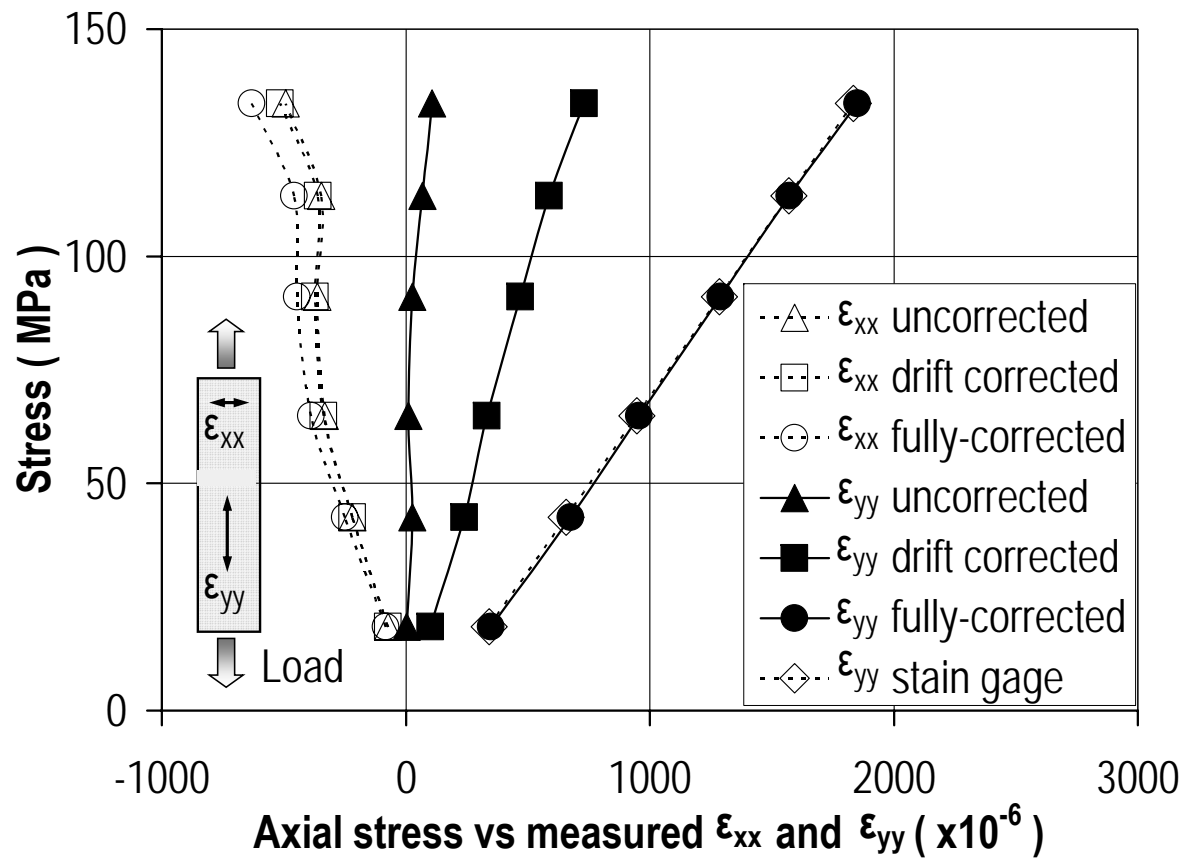


Fig. 9: Uniaxial stress versus axial strain and transverse strain for uncorrected, drift corrected and fully corrected image correlation data.